Deep Generative Modeling for Probabilistic Electricity Price Forecasting

by

Nicholas Elsasser

B.S., University of Colorado Boulder, 2022

A thesis submitted to the

Faculty of the Graduate School of the

University of Colorado in partial fulfillment

of the requirements for the degree of

Masters of Science

Department of Computer Science

2023

Committee Members:

Claire Monteleoni, Chair

Sriram Sankaranarayanan

Kyri Baker

Elsasser, Nicholas (M.S., Computer Science)

Deep Generative Modeling for Probabilistic Electricity Price Forecasting

Thesis directed by Prof. Claire Monteleoni

Electricity price forecasting in deregulated nodal electricity markets is a significant problem for market operators and market participants. Uncertainty in key market factors can propagate to significant price events that prove difficult to predict and hedge against. In this work, we propose and investigate a joint conditional probabilistic methodology for day-ahead price forecasting across a set of geographically distributed price nodes using deep normalizing flow density estimators. We motivate and assess strategies that can be used to improve and adjust probabilistic forecast results and compare our proposed methodology against open-access state-of-the-art statistical and machine learning benchmarks in energy price forecasting literature as well as a physics-based, commercially available optimal economic dispatch forecasting tool.

Dedication

To my Mother, Father, and Sister.

Acknowledgements

I would like to express special thanks to Prof. Claire Monteleoni[1] , Dr. David Kozak[2] , and Dr. Matthew Parno[3] for their guidance and mentorship. I would also like to thank the members of my research groups at both CU and Solea for their support, engaging discussions, and excellent feedback.

Datasets were kindly provided by Solea Energy LLC.

[1] University of Colorado, Boulder
[2] Solea Energy
[3] Solea Energy

Contents

Chapter

1 Introduction **1**

1.1 Dual-Settlement Nodal Electricity Markets 1

1.2 The Application of Machine Learning to Energy Price Forecasting 3

1.3 Motivation and Contributions 3

1.4 Related Work 6

2 Mathematical Background **8**

2.1 Measure Transport 8

2.2 Normalizing Flows 9

2.3 Conditional Invertible Neural Networks 10

2.4 Generative Adversarial Networks 12

2.5 Flow-GAN 13

3 Methodology **14**

3.1 Day-Ahead Forecasting Strategy 14

3.2 Datasets 16

3.3 Data Pre-Processing 17

3.4 Baselines 18

3.4.1 LASSO Estimated Auto-Regressive Model 18

3.4.2 Deep Neural Network 19

3.4.3 Commercial Optimal Powerflow Solver 20
3.5 Evaluation Metrics 20

4 Experiments **23**
4.1 Capturing Non-Stationary Prices 23
4.2 Improving Sampling Tasks with Adversarial Loss 27
4.3 Comparison Against Baselines 32

5 Conclusions **37**

Bibliography **39**

Appendix

A List of PJM Price Nodes **42**

B List of PJM Load Zones **44**

C List of NOAA Weather Stations **45**

D Model and Optimizer Hyperparameters **47**
D.1 cINN 47
D.2 GAN Discriminator 48
D.3 EPF-DNN 48
D.4 Adam Optimizer 48

Tables

Table

4.1 Comparison of strategies for handling non-stationary data 28

4.2 Results of adversarial loss inclusion 29

4.3 Count of forecasts with excessive uncertainty 31

4.4 Proposed density forecasts v.s. open-access literature point forecasts 34

4.5 Proposed density forecasts v.s. commercial optimal powerflow solver point forecasts 36

D.1 cINN Hyperparameters 47

D.2 SN-GAN Discriminator Hyperparameters 48

D.3 EPF-DNN Hyperparameters 48

D.4 Adam Hyperparameters 49

Figures

Figure

1.1 Contour map of PJM DA LMPs at various times over a single market-day 4

2.1 Conditional normalizing flow density estimator on 2-d synthetic data 11

3.1 Proposed forecasting methodology in relation to the day-ahead forecasting timeline . 15

4.1 Quarterly aggregated day-ahead prices v.s. natural gas spot prices 25

4.2 Total aggregate load v.s. day-ahead prices 25

4.3 Total aggregate wind generation v.s. day-ahead prices 26

4.4 Samples drawn joint density forecast with extreme outliers 30

4.5 Mode-covering and mode-collapsed density estimators on 2-d synthetic data 32

4.6 Mapping of the reference domain under the push-forward operation for a density estimator on 2-d synthetic data 33

4.7 Timeseries of observed v.s. forecast prices over 2/12/21-2/17/21 and 8/13/21-8/18/21 35

4.8 Density forecasts v.s. point forecasts v.s. observed prices on 8/13/21 hours 4, 12, 16, and 20 35

Chapter 1

Introduction

1.1 Dual-Settlement Nodal Electricity Markets

The increasing integration of renewable energy sources into the electrical grid has led to heightened volatility and uncertainty in electricity prices. This presents a major challenge for electricity market participants, who must be able to accurately forecast electricity prices to make informed investment and trading decisions. To address this challenge, the application of machine learning, and in particular deep generative models, to day-ahead electricity price forecasting has become a topic of significant interest.

The North American electrical grid, sometimes regarded as the "world's largest machine," is a feat of modern engineering and operations that provides a critical resource for over 400 million individuals. While the planning, construction, and maintenance of the physical infrastructure are non-trivial tasks, post-completion the continuous and efficient operation of grid resources poses perhaps an even greater challenge. To keep generation and demand synchronized, a grid operator must dispatch the least-cost optimal generators such that all electrical loads are *exactly* satisfied. Furthermore, the matching must be done continuously despite uncertainty in the load, weather, generation, grid topology, fuel prices, etc., lest there be a catastrophic failure in overall grid operations [3].

The early grid was operated by local, vertically integrated utilities that owned all the generation and transmission in an area. Due to the small scale of the grids and relative certainty in the generation mix, real-time dispatch remained simple enough such that it could be done man-

ually. Growth in the size and interconnection of the grid network has exacerbated the nonlinear and unpredictable interactions between transmission components in an alternating-current (AC) network [26]. More recently, increased penetration of renewable energy sources, such as solar and wind generation, coupled with a lack of suitable storage options has dramatically increased overall uncertainty in grid operations. One proposed solution to these challenges is the deregulation of the wholesale energy market with the development of the locational marginal price (LMP) model and competitive bid-based markets. Roughly two-thirds of U.S. electricity consumers live in a region serviced by such markets, and similar efforts are actively pursued in European energy markets under the moniker "energy liberalization."

These new, competitive energy markets allow electricity generators to offer their capacity for sale to load-serving entities, such as utilities and large energy consumers. These markets are organized by independent system operators (ISOs), which are responsible for ensuring the reliability of the electrical grid and fair markets for participants. ISOs offer multiple different markets, typically defined by the time frame of trades, to allow participants to hedge against price volatility. One example is the day-ahead (DA) market, a forward market where electricity is traded on the day immediately prior to delivery. Generators submit bid-curves stating how much they can produce and at what price, and load-serving entities (LSEs) such as utilities bid their customer's forecasted demand into the markets. Speculators play a purely financial role which works to assume excess risk that is unpalatable to LSEs and generators. After the trades are cleared and aggregated, the ISO uses a security-constrained economic dispatch (SCED) model to create generator dispatch schedules and formulate LMPs at locations on the grid referred to as *price nodes*. The LMP can be decomposed into the *energy price*, *congestion price*, and *loss price* which respectively are the costs of producing the energy (equal at all nodes), the costs of safely transmitting energy across the grid, and the energy loss due to physical transmission inefficiencies. Figure 1.1 captures a subset of LMPs in the Pennsylvania-New Jersey-Maryland (PJM) ISO over the duration of a typical market-day. Observe the uniform LMPs in the early morning hour of the market (top-left) and the significant differences between nearby prices nodes in the afternoon hours (bottom-left) indicating

low-congestion and high-congestion regimes respectively.

1.2 The Application of Machine Learning to Energy Price Forecasting

The complicated task of forecasting nodal LMPs play a crucial role in the functioning of DA markets. Accurate forecasts allow market participants to make informed trading decisions, plan generation and demand schedules, and manage risk exposure. Thus, poor forecasts can result in reduced market efficiency, realized as wasted generation resources, high energy prices, and potentially greater carbon emissions [21]. Factors such as volatile renewable generation, weather patterns, fuel prices, demand uncertainty, and complex interactions between grid components make it a formidable challenge. However, recent developments in machine learning, in particular deep learning methods, and access to historical market data show promise at capturing the complex and dynamic structures essential for accurate forecasts.

1.3 Motivation and Contributions

We motivate the development of probabilistic forecasting methods by first discussing the limitations of common point or interval forecasts. Point forecasts, despite common usage, provide the least amount of information for decision-makers to act upon, as all uncertainty is discarded to obtain a single value. In comparison, interval forecasts, when paired with point forecasts, are substantially more informative. The uncertainty surrounding a point forecast can often be captured as a confidence interval (CI), i.e. a range of estimates which likely contain the "true" value for some confidence level. The size of an interval can give decision-makers insight into the uncertainty of the forecast as "wider" CIs indicate more uncertain forecasts. Depending on the interpretations of the forecasts, the relationship between a combination of point and interval forecasts can also provide insight into the uncertainty structure. For example, a point estimate of the mean forecast near the bounds of an interval forecast may indicate certain skewness and tail behavior of the underlying forecast uncertainty. However, interval forecasts still discard valuable structural information such as multi-modality and tail behavior outside the interval range.

Figure 1.1: Nodal day-ahead LMPs and the contours interpolated prices in areas between nodes. White circles depict the location of target price nodes in PJM whose prices are reflected in the inscribed colors. Prices between nodes are interpolated using radial-basis-function kernel interpolation.

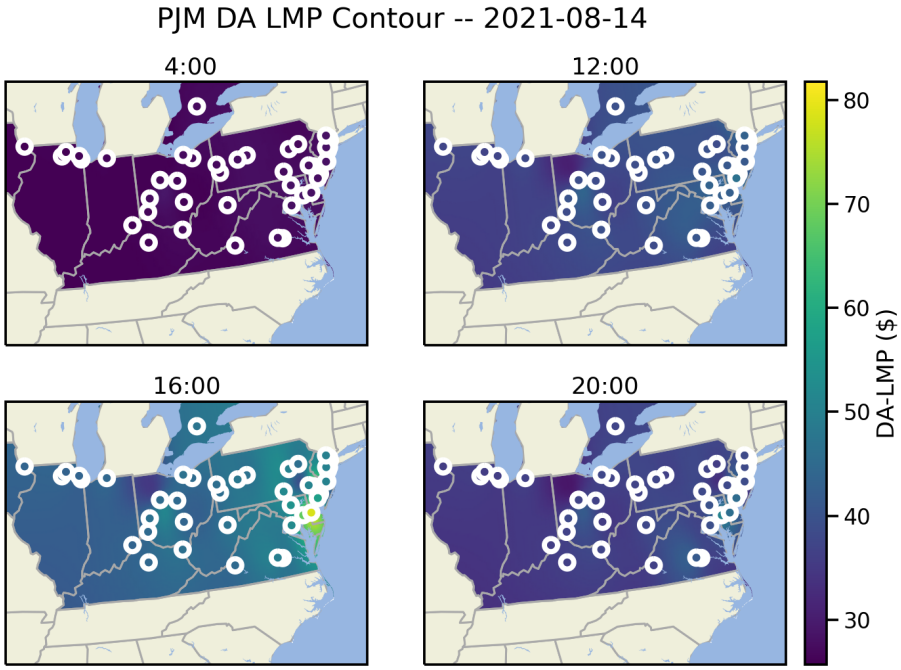

Capturing all complexities and nuances of forecast uncertainty can only be achieved with probability density forecasts, whereby a probability density function is defined over the entire forecast domain. Despite powerful methods existing for low-dimensional problems, efficiently modeling joint conditional distributions in high dimensions has long been extremely difficult. Recent advances in deep neural-network-based generative models, in particular, *normalizing flows*, show promise for characterizing high dimensional and complex joint conditional probability densities. Furthermore, certain constructions of normalizing flows allow both exact likelihood evaluation and efficient sampling, which can enable powerful Monte Carlo methods to estimate key quantities of interest needed to make informed financial decisions in energy markets.

In this work, we present a novel methodology for characterizing joint conditional probabilistic DA LMP forecasts using normalizing flow generative models which can accurately capture conditional relationships between market fundamentals and resulting prices, complex spatial correlations between price nodes, and forecast uncertainty. Additionally, we investigate several techniques to improve forecasting skill against non-stationary market data and the use of generative adversarial network methods to refine performance in sampling-based tasks. We also compare the forecasting performance of our proposed methods against point forecasting open-access benchmarks from literature and a commercial optimal powerflow point forecasting product, demonstrating more accurate forecasts than comparable solutions with unmatched uncertainty quantification.

The rest of this work is structured as follows. In Chapter 2 we outline the key mathematical background required to formulate probabilistic forecasts using recent advances in deep generative modeling. In Chapter 3 we define our proposed methodology for characterizing probability density estimators and generating probabilistic forecasts. In Chapter 4 we investigate techniques to improve forecasting skill in day-ahead energy markets and compare our proposed methods against open-access benchmarks in energy price forecasting literature and commercial price forecasting tools. Finally, in Chapter 5 we summarize our key findings and lay out key future research paths to improve model results, robustness, interpretability, and generalizability.

1.4 Related Work

Energy price forecasting literature can be split roughly into three categories: *system pattern* (SP) methods, statistical and machine learning methods, and deep-learning methods.

The work of Zhou et al. [31] develop the idea of SPs as an exploitation in the structure of the LMP optimization problem formulation, where predictable market characteristics and associated *system pattern regions* (SPRs), or continuous neighborhoods of market conditions represented by polytopes in load space, give rise to specific predictable SPs. Forecasting price action is then reduced to estimating which SPRs future market conditions will map to, and subsequently retrieving the likely SPs and price action. To overcome bias in the set of observed market states, a "probabilistic" formulation is also presented that can report upper and lower quantile forecasts along with a mean forecast. However, the SPR state space suffers from the curse of dimensionality, making analysis of large grids computationally intractable. Geng et al. [7] build upon the SPR concept, showing that they can be constructed using data-driven methods, in particular learning SPR classification boundaries with support vector machines. These data-driven SPR techniques are, however, still computationally intractable for anything more than small, synthetic grid examples. Radovanovic et al. [20] expand upon a similar idea to SPRs. Through the use of recent advances in compressed sensing they reconstruct grid topologies allowing downstream inference and clustering of congestion prices. Clusters of generation-mix and load forecast are mapped to price clusters allowing for LMP forecasting. The SPR-like representations make this method significantly more scalable for inference, however, training the model incurs a costly step of reconstructing grid topology which can be significant for large grids [12].

Using traditional statistical methods and machine learning methods, Uniejewski et al. [22] propose a linear auto-regressive model using ordinary least squares regression and LASSO automatic feature selection techniques. This linear model can be modified for quantile regression tasks [23] or with advanced jump-diffusion and time-series techniques to produce probabilistic forecasts [19]. Andrade et al. [1] present a methodology for both point and quantile forecasts using robust gradi-

ent boosting trees and linear quantile regression, coupled with post-processing that exploits daily average prices to increase forecast quality.

Deep-learning methods have recently risen in popularity for energy forecasting, beginning with the work of Wang et al. [25] who present a stacked de-noising auto-encoder (SDA) neural network with unsupervised pre-training and supervised fine-tuning regimes to improve forecast accuracy. Subsequent work by Lago et al. [16] compare novel deep feed-forward neural network (DNN), convolution neural network (CNN), and recurrent neural network (RNN) architectures and demonstrate the superiority of deep-learning methods over traditional statistical methods. A two-stage convolutional long short term memory (CLSTM) neural network to first forecast generation bid curves to improve second-stage LMP point forecasts is proposed in [29]. Zhang et al. [30] introduce a generative adversarial network (GAN) using a novel 3d tensor structure and convolutional neural network to learn the spatiotemporal interactions from the tensor representation. Cramer et al. [4] develop a normalizing flows model to capture the joint probability distribution of multi-hour price action on a single node and generate probabilistic forecasts for intra-day nodal prices in the German EPEX spot market.

Chapter 2

Mathematical Background

2.1 Measure Transport

A family of methods for density estimation fall under the umbrella term of *measure transport*. Let $\pi : \mathbb{R}^n \mapsto \mathbb{R}^+$ refer to the *target density* that we wish to estimate and $\eta : \mathbb{R}^n \mapsto \mathbb{R}^+$ refer to a known *reference density* with which we can evaluate likelihoods and draw samples from. If π and η both are smooth and continuous over $\mathbb{R}^n$ then there is a smooth bijection (diffeomorphism) $T : \mathbb{R}^n \mapsto \mathbb{R}^n$, referred to as a transport map, such that the following change of variables relationship holds,

$$\pi(x) = \eta\left(z = T^{-1}(x)\right) \left|\det J_T(x)\right|^{-1},$$

where $J_T(x)$ is the Jacobian matrix of T evaluated at x. We refer to the operation $z = T^{-1}(x)$ as a *pull-back* of x in target-space to the associated z in reference-space. It is then clear that the likelihood of observing some x under π can be evaluated by a pull-back operation to find the associated z and evaluating the likelihood of z under η. Note that $\left|\det J_T(x)\right|^{-1}$ must be used to normalize changes in volume incurred by T to retain a valid probability density function; as such, it is important for T to have a tractable Jacobian determinant[1] . Sampling $x \sim \pi$ can be accomplished by drawing a sample $z \sim \eta$ and evaluating the analogous *push-forward* operation $x = T(z)$.

[1] Or more aptly, a tractable log Jacobian determinant as evaluating log-likelihoods tends to be more numerically stable.

Typically, the true forms of π and T must be estimated. Let $f_\theta : \mathbb{R}^n \mapsto \mathbb{R}^n$ be a diffeomorphism parameterized by θ with the resulting density estimator π_θ. The optimal parameters, θ^*, are those that minimize the difference between π_θ and π. We quantify the difference between π_θ and π using the Kullback-Leibler divergence [15], defined for two densities P and Q as $D_{\mathrm{KL}}(P||Q) = \int P(u) \log \frac{P(u)}{Q(u)} du$.

$$\begin{aligned} D_{\mathrm{KL}}(\pi||\pi_\theta) &= \int \pi(u) \log \frac{\pi(u)}{\pi_\theta(u)} du \\ &= -\int \pi(u) \log \pi_\theta(u) du + \int \pi(u) \log \pi(u) du \\ &= -\mathop{\mathbb{E}}_{u\sim\pi} [\log \pi_\theta(u)] + \mathop{\mathbb{E}}_{u\sim\pi} [\log \pi(u)] \\ &= -\mathop{\mathbb{E}}_{u\sim\pi} \left[\log \eta \left(z = f_\theta^{-1}(u)\right) - \log \left|\det J_{f_\theta}(u)\right|\right] + \mathop{\mathbb{E}}_{u\sim\pi} [\log \pi(u)] \end{aligned} \tag{2.1}$$

$\mathop{\mathbb{E}}_{u\sim\pi} [\log \pi(u)]$ is constant with respect to θ. Furthermore, over a collection of N samples, $\{x_i\}_{i=1}^N \sim \pi$, first expected value of (2.1) may be approximated with a Monte-Carlo integral,

$$\mathcal{L}_{\mathrm{MLE}}(\theta) = -\frac{1}{N} \sum_{i=1}^{N} \log \eta \left(z = f_\theta^{-1}(x_i)\right) + \log \left|\det J_{f_\theta}(x_i)\right|. \tag{2.2}$$

We recognize (2.2) as *maximum-likelihood loss*. Thus, minimizing the KL-divergence between π and π_θ is approximated by maximizing the likelihood of our observations under π_θ.

2.2 Normalizing Flows

Many characterizations of f_θ exist, with those using deep neural networks typically referred to as *normalizing flows*. There are many specific normalizing flow implementations. We only expand upon a variation called *discrete-time affine-coupling flows* popularized by Real-NVP [5]. For a review of current normalizing flow methods refer to [14].

The *discrete-time affine-coupling flows* constructs f_θ as the composition of L smooth and invertible functions, $f_\theta(u) = f_{\theta_L} \circ f_{\theta_{L-1}} \circ \cdots \circ f_{\theta_1}(u)$, with each $f_{\theta_\ell} : \mathbb{R}^n \mapsto \mathbb{R}^n$, $\ell \in [1, L]$ referred to as an *affine-coupling block*. Each coupling block function $v = f_{\theta_\ell}(u)$ has the following form: First

splitting the components of u into two equally sized partitions $u = [u_1 \;\; u_2]$,

$$v_1 = u_1,$$
$$v_2 = u_2 \odot \exp(s(u_1)) + t(u_1).$$

Consequently, $v = [v_1 \;\; v_2]$. Functions s and t are neural networks referred to as the *scale* and *transform* networks respectively whose parameters are collectively exhaustive subsets of θ_ℓ. The structure of the affine coupling block leads to a lower-triangular Jacobian, whose log-determinant is the sum over the components from the output of s.

Affine coupling flows may limit the interactions between certain subsets of components. For instance, partitioning the input by the first and second halves for all coupling blocks would result in applying the identity to the first half of the components likely resulting in a poor density estimator. Adequate "mixing" of components can be accomplished by permuting the components between flow layers, achieved generally through random orthonormal projections or 1x1 convolutional filters, depending on the architecture of the model and application domain.

2.3 Conditional Invertible Neural Networks

The conditional invertible neural network (cINN) [2] is a further development of the Real-NVP architecture that improves the expressiveness of each flow layer and adds support for conditional density estimation.

Similar to Real-NVP, a composition of L functions interspersed with $L-1$ component permutations is constructed. Let $c \in \mathbb{R}^m$ be the conditional quantities and $v = f_{\theta_\ell}(u; c)$ be a *conditional coupling block* with the following structure,

$$v_1 = u_1 \odot \exp\left(s_1(u_2; c)\right) + t_1(u_2; c)$$
$$v_2 = u_2 \odot \exp\left(s_2(v_1; c)\right) + t_2(v_1; c).$$

Functions s_1, s_2, t_1, and t_2 are neural networks whose parameters are collectively exhaustive subsets of θ_ℓ. The definition of f_{θ_ℓ} enables efficient calculation of the log Jacobian-determinant as the sum over the components of the outputs from s_1 and s_2. Including c to the input of all neural networks across all coupling blocks enables conditional density estimation, however, an unconditional density estimate can be constructed without these quantities. Following from the unconditional push-forward and pull-back operation definitions, we denote $z = f_\theta^{-1}(x; c)$ as the *conditional pull-back* operation and $x = f_\theta(z; c)$ as the *conditional push-forward* operation, whose processes are illustrated in Figure 2.1.

Figure 2.1: A conditional normalizing flow comprised of three coupling blocks applied to a synthetic dataset. **Left:** samples drawn from a reference standard Gaussian distribution. **Right:** samples after the conditional push-forward operation has been applied. **Center:** intermediate transformations as the samples are pushed through the coupling blocks.

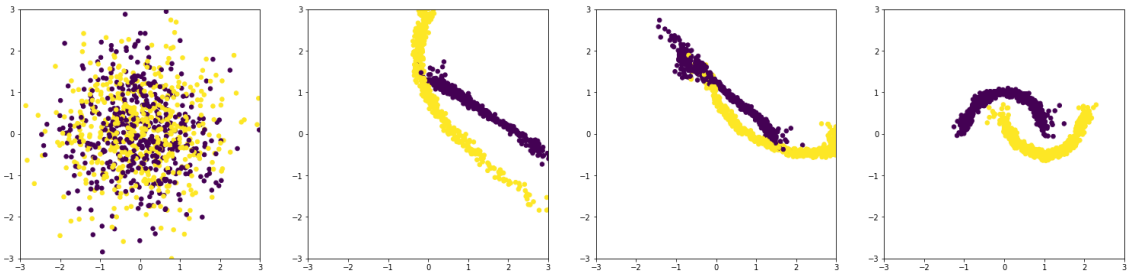

An additional optional neural network $\tilde{c} = h(c)$ is proposed as a feature extraction model that is trained end-to-end with the normalizing flow model. When in use, the coupling block input quantities c are replaced by $\tilde{c}$. The purpose of the feature extraction network is to efficiently share informative features of the conditional quantities between all flow layers in favor of each neural network in the flow model independently extracting informative features. Inclusion of the network may be important when conditioning on large, complex quantities such as images, however, it may not be beneficial when conditioning on a small number of simple quantities such as the classification of a hand-drawn digits or characters.

2.4 Generative Adversarial Networks

Generative adversarial networks (GANs) [10] are a family of deep generative models characterized by two distinct models trying to outperform one another. The goal of a generative model is to construct a probabilistic *generator* $G : \mathbb{R}^k \mapsto \mathbb{R}^n$ such that samples drawn from $x \sim G$ are "realistic" compared to those drawn from a true target distribution $x \sim \pi$. Determining if a sample is realistic (i.e. a binary classification to determine if the sample is drawn from π) is accomplished with a secondary model referred to as the *discriminator* or critic $D : \mathbb{R}^n \mapsto [0,\ 1]$. Since G and D are unknown, let G_θ and D_ϕ be functions parameterized by θ and ϕ respectively.

The objective of the discriminator is to correctly classify whether a given observation comes from G_θ or π. Estimating ϕ by maximum likelihood yields

$$\max_{\phi} \mathop{\mathbb{E}}_{x\sim\pi} \left[\log D_\phi(x)\right] + \mathop{\mathbb{E}}_{z\sim G_\theta} \left[\log\left(1 - D_\phi(z)\right)\right],$$

whose expectations can be evaluated via Monte Carlo integration over a set of training observations $\{x_i\}_{i=1}^N \sim \pi$ and a set of synthetic samples $\{z_i\}_{i=1}^N \sim G_\theta$. The objective of the generator is to generate samples that are indistinguishable from samples of π as judged by D_ϕ. Similarly, estimating θ by maximimum likelihood yields

$$\max_{\theta} \mathop{\mathbb{E}}_{z\sim G_\theta} \left[\log D_\phi(z)\right]. \tag{2.3}$$

The expected value in (2.3) is denoted as the *adversarial loss* function, $\mathcal{L}_{\text{ADV}}(\theta)$, which can likewise be approximated with a collection of synthetic samples $\{z_i\}_{i=1}^N \sim G_\theta$.

While GANs are widely used for tasks requiring high-dimensional and high-quality samples, they suffer from two key issues that can severely limit their practicality: unstable training and the phenomenon of *mode-collapse*.

Unstable training arises from the construction of the loss for both the generator and discriminator. The loss of each model is based on the parameters of the other, thus performing parameter updates during training results in new loss functions on every update. The changing objective

landscape tends to collapse or diverge during training. Significant work has gone into improving the stability of GAN training, however, achieving good results is still more art than science.

The phenomenon of *mode-collapse* is another pervasive problem of GANs, whereby the generator only learns to generate samples within a small neighborhood of the target distribution resulting in high-quality samples that lack diversity. This arises because the generator is only trained to draw samples that have high-likelihood of originating from π according to the discriminator, however, it is trivial for the generator to over-fit by generating high-quality samples only from a small region of the target distribution. An illustrative example is generating hand-drawn digits, where a *mode-covering* model would be able to generate realistic images for all digits $0 - 9$, a *mode-collapsed* model would only be able to generate realistic images for a subset of digits or only a single digit.

2.5 Flow-GAN

The Flow-GAN [11] model proposes using a normalizing flow for the generator function to overcome the two key issues presented with GANs by constructing a hybrid loss function for the generator combining both the *maximum-likelihood loss* and *adversarial loss* functions,

$$\min_{\theta} \mathcal{L}_{\text{MLE}}(\theta) - \lambda_{\text{ADV}} \mathcal{L}_{\text{ADV}}(\theta),$$

where $\lambda_{\text{ADV}} \geq 0$ is a hyperparameter used to blend the losses. Setting $\lambda_{\text{ADV}} = 0$ is equivalent to training a vanilla normalizing flows model ignoring the discriminator, while setting λ_{ADV} to a large number is equivalent to training a vanilla GAN.

Inclusion of $\mathcal{L}_{\text{MLE}}$ alleviates both unstable training and mode-collapse issues. First, the optimization landscape of $\mathcal{L}_{\text{MLE}}$ is constant with respect to the parameters ϕ and θ, thus convergence of the generator with respect to how well it captures the sample target distribution from the training observations can be monitored throughout training. Second, maximizing the likelihood of observing all training examples means mode-collapse is unlikely as any collapse during training would be heavily penalized with extremely low likelihood evaluations. amsmath

Chapter 3

Methodology

3.1 Day-Ahead Forecasting Strategy

In DA nodal markets energy prices are settled on an hourly basis. Participants are required to submit all trades — a single trade consists of a *location*, *hour*, *direction* (buy or sell), *price*, and *volume* — for a given market-day no later than one-day in advance. Specifically, if the market-day is denoted by T, there is a trade-submission deadline on the day $T-1$ at which all trades for T are submitted. For each node, prices must be forecasted for all 24 hours simultaneously. Thus, for a set of n price nodes a total of $n \times 24$ total price forecasts are required. There is no consensus on the best forecasting methodology, with popular choices being a single model creating a joint $n \times 24$ forecast [30, 29], one model per-node with 24-hour joint forecasts [1, 25, 16], one model with joint forecasts over the nodes independently per-hour [31, 7, 20], and finally one model per-hour per-node[22].

In this work, the DA price forecasting problem is approached using a single model to jointly forecast price densities across all n nodes and forecasts for each hour are generated independently. This joint probabilistic forecasting strategy captures the complex spatially-correlated price distribution between nodes for each hour given fundamental market forecasts. That is, if $\mathcal{X}_t \subseteq \mathbb{R}^n$ is a random variable with realizations x_t of the nodal LMPs for a specific market-hour t and $c_t \in \mathbb{R}^m$ is a real-valued vector of fundamental market forecasts for the same market-hour, we propose a model which characterizes the joint conditional probability distribution $p_{\mathcal{X}_t}(x_t|c_t)$. Thus when forecasting an entire market-day, 24 independent probability densities are characterized for each hour as shown

in Figure 3.1.

Figure 3.1: Proposed day-ahead forecasting methodology. At the time of the trade submission deadline 24 joint conditional distributions have been characterized for each hour of the upcoming market-day.

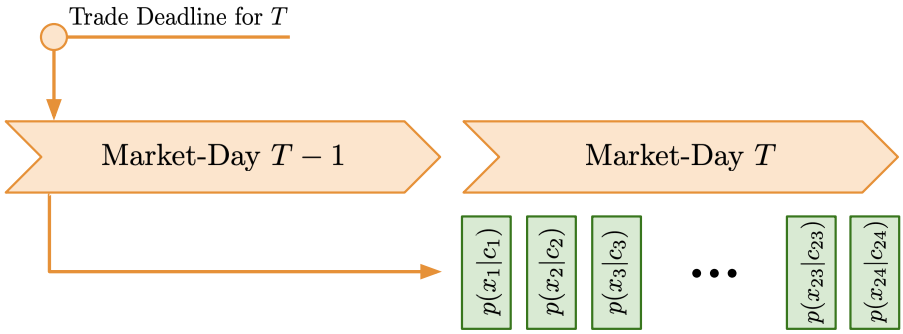

The proposed strategy to characterize the joint conditional density estimators is as follows,

(1) Select a set of n price nodes for which to generate forecasts and a set of m quantities that affect day-ahead nodal energy prices and are available before the trade submission deadline.

(2) Choose an n-dimensional probability distribution to be the reference distribution η. Typical choices are standard uniform or Gaussian distributions, however, any distribution with tractable log-likelihood evaluations and sampling capabilities could be used.

(3) Construct a diffeomorphism $f_\theta : \mathbb{R}^n \mapsto \mathbb{R}^n$ characterized by the cINN architecture described in Section 2.3. Additionally, a suitable feature extraction network $h(c_t)$ should be chosen. Omission of the feature extraction network is equivalent to $h(c_t) = \mathbf{I}c_t$ where $\mathbf{I}$ is the $m \times m$ identity matrix. Note that the feature extraction network and its respective parameters are included when referring to f_θ.

(4) Construct a discriminator $D_\phi : \mathbb{R}^{n+m} \mapsto [0,\ 1]$ with which to evaluate $\mathcal{L}_{\text{ADV}}$, and select a value for λ_{ADV} to control the emphasis on $\mathcal{L}_{\text{MLE}}$ or $\mathcal{L}_{\text{ADV}}$ in the hybrid loss function.

(5) Update the parameters of f_θ and D_ϕ using the Adam stochastic gradient descent algorithm [13]. Mini-batches of pairs from the set of N historical training observations

$\{(x_i,\ c_i)\}_{i=1}^{N}$ are used to evaluate $\mathcal{L}_{\text{MLE}}$. Samples $\{z_i\}_{i=1}^{N} \sim \eta$ are drawn and the conditional push forward operation is applied to form synthetic price samples $\hat{x}_i = f_\theta(z_i; c_i)$. Mini-batches of pairs from the resulting set $\{(\hat{x}_i,\ c_i)\}_{i=1}^{N}$ are used to evaluate $\mathcal{L}_{\text{ADV}}$. Note the conditional quantities are identical in both the real and synthetic mini-batches.

3.2 Datasets

- **Prices**: Historical day-ahead LMP time-series are obtained for 45 price nodes in the PJM market capturing prices in all 25 load zones and the interconnections with neighboring markets. These prices are published by PJM on an hourly basis shortly after the trade submission deadline for the upcoming market-day has passed. The full list of nodes can be found in Appendix A.

- **Load Forecasts**: Historical hourly load forecasts are obtained for each of the 25 load zones in PJM. Zonal load forecasts represent the expected energy demand in megawatts (MW) in each sub-region of PJM for a given market-hour and are published on an hourly basis by PJM. These forecasts are available for participants to use during trade generation and submission. The full list of load zones can be found in Appendix B.

- **Wind Generation Forecasts**: A historical hourly time-series is obtained for the ISO-level wind generation near-term forecast. This forecast is published by PJM and represents the expected total generation (MW) from all wind turbine renewable power plants in PJM for a given market-hour and is available to participants during trade generation and submission.

- **Meteorological Forecasts**: Historical hourly meteorological forecasts are obtained for a collection of NOAA weather stations in and around PJM. There are a total of 52 weather stations spanning the entire geographical region of PJM. Each weather station reports expected hourly wind speeds (mph), temperature (°F), and dew-point (°F). These forecasts are available to participants during trade generation and submission. The full list of NOAA weather stations can be found in Appendix C.

- **Natural Gas Prices**: Historical natural gas spot price time-series are obtained for the TETCO-M3 hub. The prices reflect the daily volume-weighted-average-price (VWAP) and are reported daily. The daily VWAP for the upcoming market-day is unknown, so instead the most recent daily VWAP at the time of trade-generation is persisted and used for all 24 hours in the price forecast.

Time-series for all of the above datasets are captured for the entirety of years 2019, 2020, and 2021.

3.3 Data Pre-Processing

To improve the numerical stability of the stochastic gradient descent algorithm we preprocess all aforementioned quantities to normalize the disparate scaling between feature classes. A standard linear scaling strategy on a per-quantity basis was found to be sufficient when applied to all quantities despite more complex variance stabilizing scaling strategies proposed in energy forecasting literature [24]. Let $\{y_i\}_{i=1}^{N}$ be a historical time-series for a scalar quantity such that the first $k < N$ values are used for model training and the remaining values are held out for validation, then the transformation $\bar{y}_i = \frac{y_i - \hat{\mu}_y}{\hat{\sigma}_y}$ is applied for $1 \leq i \leq N$ where $\hat{\mu}_y,\ \hat{\sigma}_y$ are the empirical mean and standard deviation of the training set for the respective quantity.

In addition to the scaled fundamental market forecasts, temporal encodings of the upcoming market-time t are constructed. Assuming t contains information on the hour-of-day and elapsed-days-since-epoch (1-1-1970), given by $\text{hour}(t) \in \{1, 2, \ldots, 24\}$ and $\text{day}(t) \in \mathbb{N}$ respectively, we construct the following three sinusoidal encodings to relate temporally similar observations,

$$\begin{aligned}
\text{Hour-of-Day} &= \left[\cos\left(\text{hour}(t) \times \frac{2\pi}{24}\right),\ \sin\left(\text{hour}(t) \times \frac{2\pi}{24}\right)\right] \\
\text{Day-of-Week} &= \left[\cos\left(\text{day}(t) \times \frac{2\pi}{7}\right),\ \sin\left(\text{day}(t) \times \frac{2\pi}{7}\right)\right] \\
\text{Day-of-Year} &= \left[\cos\left(\text{day}(t) \times \frac{2\pi}{365}\right),\ \sin\left(\text{day}(t) \times \frac{2\pi}{365}\right)\right].
\end{aligned}$$

Note that we are targeting forecasts on 45 price nodes, thus the reference and target distributions are 45-dimensional, however, the affine coupling block architecture requires an even number of dimensions for the component partitions to be of equal sizes. To remedy this, a dummy dimension is created by appending zeros to the price-vector observations bringing the number of dimensions up to 46. When sampling price forecasts, values from the dummy dimension are dropped after applying the push-forward operation.

3.4 Baselines

To validate the results of our proposed forecasting methodology we compare against the following three point-forecast baselines. Note that the first two baselines come from the open-source `epf-toolbox` [17] python library, however, the models provided in this toolbox are meant to be trained on the datasets provided by this toolbox. The dataset available for PJM only includes day-ahead prices for three price nodes and load forecasts for a single load zone and the total system-wide load. As such, the models are modified to use all available exogenous quantities and the proposed data pre-processing methodologies, however, the proposed sinusoidal temporal encodings are omitted in favor of the temporal encodings originally defined in the `epf-toolbox`.

3.4.1 LASSO Estimated Auto-Regressive Model

The *LASSO estimated auto-regressive* (LEAR) model is a parameter-rich auto-regressive model with the capacity to handle exogenous variables. Let $d(t)$ and $h(t)$ be shorthand for the functions $\text{day}(t)$, $\text{hour}(t)$ respectively for a market-time t, $p_{d(t)} \in \mathbb{R}^{24}$ be the realized day-ahead price at a single price node at market-times on the same day as $d(t)$, $x^j_{d(t)} \in \mathbb{R}^{24}$ be the j^{th} exogenous quantity at market-times on the same market-day as $d(t)$, and $\mathbf{e}_j$ the j^{th} column of the 7×7 identity matrix. Then the forecast $\hat{p}_t$ for an upcoming market-time t at a single node is defined as,

$$\begin{aligned}\hat{p}_t(\theta) = &\sum_{k\in\{1,2,3,7\}} {\theta^0_{[24\times(k-1):24\times k]}}^{\mathsf{T}} p_{d(t)-k} \\ &+ \sum_{j=1}^{m} {\theta^j_{[0:24]}}^{\mathsf{T}} x^j_{d(t)} + {\theta^j_{[24:48]}}^{\mathsf{T}} x^j_{d(t)-1} + {\theta^j_{[48:96]}}^{\mathsf{T}} x^j_{d(t)-7} \\ &+ {\theta^{m+1}}^{\mathsf{T}} \mathbf{e}_{[d(t) \mod 7]} \\ &+ \epsilon,\end{aligned}$$

where $\theta^k \in \mathbb{R}^r$ are parameters with transpose $\theta^{\mathsf{T}} \in \mathbb{R}^{1\times r}$ and parameters $\theta^k_{[i:j]}$ are a subset of parameters θ^k characterized by the entries spanning the interval $[i, j)$ with $0 < i < j \leq r$, and $\theta^{\mathsf{T}} = [{\theta^0}^{\mathsf{T}} \dots {\theta^{m+1}}^{\mathsf{T}}]$ is the full set of parameters for the LEAR model. In this definition, θ^0 are auto-regressive parameters, $\theta^1 \dots \theta^m$ are parameters for exogenous variables, and θ^{m+1} are parameters for a day-of-the-week temporal one-hot encoding. ϵ is a standard error term.

The LEAR model is trained using sum-of-squares loss between the forecasted price $\hat{p}_t$ and the realized price p_t applying a ℓ_1 weight penalty with intensity $\lambda \geq 0$ on parameters θ to encourage sparsity. Note, θ is optimized only for a single hour, thus when training only observations at a specific hour are considered. Over a set of N training days, θ_h is optimized for a specific market hour h as,

$$\min_{\theta_h} \sum_{d=1}^{N} \left(\hat{p}_{t=(d,h)}(\theta_h) - p_{t=(d,h)}\right)^2 + \lambda\|\theta_h\|_1.$$

3.4.2 Deep Neural Network

The *deep neural network* (DNN) model is a multi-layer perceptron (MLP) neural network that produces point forecasts for a single node at all 24 market-hours simultaneously. The DNN is trained on the same quantities as the LEAR model, that is for the upcoming market-day d, the neural network forecasts the price vector $\hat{p}_d$ using price history $\{p_{d-1}, p_{d-2}, p_{d-3}, p_{d-7}\}$, exogenous forecasts and history $\left\{x^j_d, x^j_{d-1}, x^j_{d-7}\right\}$ for exogenous quantities $1 \leq j \leq m$, and temporal encoding $\mathbf{e}_{[d \mod 7]}$. The DNN is trained using root-mean-squared (RMS) loss, and a full description of

hyperparameters can be found in Appendix D.

3.4.3 Commercial Optimal Powerflow Solver

The commercial optimal powerflow solver (OPF) is a tool that produces joint point LMP forecasts over a set of nodes for a single hour by solving a variation of the *security constrained economic dispatch* (SCED) optimization problem. The process by which LMPs are actually produced is derived from a solution to this problem, and the OPF tool aims to forecast the parameters of the SCED problem such that its solution yields price forecasts. Explanation of SCED and related power system optimization problems are beyond the scope of this work, however a review of these problems and the tools used to solve them can be found in [32]. Forecasts from commercial OPF tools are often highly desirable for their accuracy and because they are derived from the true physical properties underpinning grid and market behavior.

3.5 Evaluation Metrics

Root-mean-squared-error (RMSE), mean-absolute-percentage-error (MAPE) and mean-absolute-error (MAE) are common metrics in energy price forecasting literature, however, they are only valid for use with point forecasts. Of those metrics, MAE is the best metric for energy price forecasts because the linear errors best represent the actual losses one would incur when trading — that is the profit or loss incurred on a trade scales linearly with the difference between the buy and sell prices, analogous to the absolute error between realized and forecasted prices. Using these metrics for our forecasts would require the distillation of the information-rich probabilistic forecasts down into point forecasts. Instead, we use the *continuous ranked probability score* (CRPS) [9], which generalizes the absolute error metric to probabilistic forecasts. Let $\mathbb{1}_{[x \in A]}$ be an indicator which takes the value 1 when $x \in A$ and 0 otherwise. For a univariate random variable $\mathcal{X} \subseteq \mathbb{R}$ with the probabilistic forecast represented by the cumulative density function $F_{\mathcal{X}}$, the CRPS of $F_{\mathcal{X}}$ against a realization $y \in \mathbb{R}$ is defined as

$$\mathrm{CRPS}_{F_{\mathcal{X}}}(y) = \int_{-\infty}^{\infty} \left(F_{\mathcal{X}}(u) - \mathbb{1}_{[y \leq u]}\right)^2 du. \tag{3.1}$$

We may interpret (3.1) as the mean squared error between the forecast c.d.f. and the c.d.f. given by a Dirac delta function at the realized value. The CRPS generalizes the absolute error of a point forecast, illustrated by the substitution of $\mathbb{1}_{[x \leq u]}$ for $F_{\mathcal{X}}(u)$ given a point forecast x,

$$\int_{-\infty}^{\infty} \left(\mathbb{1}_{[x \leq u]} - \mathbb{1}_{[y \leq u]}\right)^2 du = \int_{\min(x,y)}^{\max(x,y)} du = |x - y|,$$

thus enabling direct comparison of probabilistic and point forecasting methods. A computation-friendly equivalent expression can also be derived,

$$\mathrm{CRPS}_F(y) = \mathbb{E}\left[X - y\right] - \frac{1}{2}\mathbb{E}\left[X - X'\right], \tag{3.2}$$

where X and X' are i.i.d. from a distribution with c.d.f. F.

In practice, the marginal c.d.f.s of each price node are inaccessible. Instead, a set of M samples are drawn from the joint conditional density estimator the empirical marginal c.d.f of the j^{th} price node, $\hat{F}_{\mathcal{X}^j}$, is computed as

$$\hat{F}_{\mathcal{X}^j}(u) = \frac{1}{M}\sum_{i=1}^{M} \mathbb{1}_{[x_i^j \leq u]}. \tag{3.3}$$

From which we estimate the CRPS on the j^{th} price node, $\widehat{\mathrm{CRPS}}_{\hat{F}_{\mathcal{X}}^j}$, by the substitution of (3.3) into (3.1)[1].

As this CRPS metric is only defined for univariate distributions, univariate forecasts for each price node are obtained by marginalizing samples drawn from the entire joint distribution. The average CRPS score over all price nodes for a single hour t, denoted here as mCRPS, is taken as a single distilled metric directly comparable to the MAE of a point forecast at hour t averaged over the price nodes.

[1] Note that the forms of the CRPS metric presented here are biased estimators. For a description of an unbiased counterpart and comparisons between various estimators refer to [28]. In our computations we used an unbiased counterpart to (3.2), however, for the remainder of this paper we continue to reference the estimator characterized by the substitution of (3.3) into (3.1) as we believe the relevant behavior is clearest in this form.

$$\widehat{\mathrm{mCRPS}}_{\mathcal{X}_t}(y) = \frac{1}{n}\sum_{j=1}^{n} \widehat{\mathrm{CRPS}}_{\hat{F}_{\mathcal{X}_t^j}}(y^j) \tag{3.4}$$

Additionally, the median and 99%-ile *negative log-likelihood* (NLL) metrics are evaluated on the validation dataset. A natural question is why use the median and 99%-ile NLL scores when the typical metric is the mean NLL (equivalent to $\mathcal{L}_{\mathrm{MLE}}$). We found that despite being a valuable metric for training and parameter updates, tracking and evaluating mean NLL was unstable on our dataset due to outlier sensitivity. We would often experience a small set, or even a single validation example, that would have incredibly large NLL values causing the mean calculations to be biased by the outliers leading to unstable results making fair model comparisons difficult. Tracking median NLL values was found to be better for model comparisons as the metric is robust to outlier examples. The inclusion of the 99%-ile NLL proves useful as a large 99%-ile error implies the model is poorly fit beyond a handful of outlier observations. While certain regularization techniques we found to help reduce this behavior, we still consider it an open problem for future research to analyze model sensitivity and determine methods to improve robustness against these outlier evaluations.

Chapter 4

Experiments

The same cINN normalizing flow architecture, spectral-normalized GAN (SN-GAN) [18] discriminator architecture, and Adam optimizer parameters between all experiments. The details of the common model and optimizer hyperparameters are listed in Appendix D. The dataset is split into 2019 and 2020 solely for training and 2021 is held out for evaluation. A strict backtesting procedure is followed, where a model producing forecasts for an upcoming market-day has only been trained on data that would be available to a real participant prior to the market-day.

All models in this work were trained on an NVIDIA GTX 1060–6GB GPU using Python v3.10.8 and PyTorch v1.13.0. While GPU training allowed larger batch sizes and accelerated training times, often under 10 minutes, these models can be trained on CPU with smaller batch sizes, often taking between 10-30 minutes (tested on an AMD Ryzen 3700x @ 3.6GHz with 16GB RAM and a 2020 Intel i7 @ 2.3GHz 13-inch Apple Macbook-Pro with 16GB RAM).

4.1 Capturing Non-Stationary Prices

Changes in market fundamentals over time lead to non-stationary price distributions, with key factors including: *grid topology*, *fuel prices*, *population and load patterns*, *generator outages*, *renewable penetration*, *generation mix*, *weather patterns*, etc. Much of the variation in energy prices can be explained by changes in the fundamentals of the dataset, for example, the relationship between energy prices and gas prices as shown in Figure. 4.1, seasonal load patterns as shown in Figure 4.2, or seasonal generation mixes shown in Figure 4.3. However, while a well-calibrated

model can capture the complex, nonlinear relationships of these quantities with the powerful capacities provided by deep learning methods, these interactions change over time, and with respect to inaccessible quantities such as grid topology. Thus, energy price forecasting methods must accurately track the non-stationary distributions and quickly adapt as new data becomes available. For the experiments in this section note $\lambda_{\text{ADV}} = 0$.

The following three strategies are proposed for increasing the forecasting skill on non-stationary energy market data:

(1) **Parameter recalibration.** Parameter recalibration (PR) is a common tool used in time-series forecasting whereby after some amount of time has passed and new data has become available the parameters of the forecasting model are updated using the new observations. Let $T \in \mathbb{N}^+$ be a hyperparameter representing the number of market-days between recalibrations. The model will produce a set of forecasts for a single T-day interval using fixed parameters, after which, the observations in the T-day interval are added to the training set and the model is re-trained from scratch on the extended history. $T = 1$ is equivalent to re-training the model from scratch each day before trade submission while $T \geq 365$ is equivalent to never recalibrating over the entirety of 2021.

(2) **Rolling training windows.** Rolling training data windows (RT) are another common timeseries forecasting tool when old data is assumed to be "less predictive" than the most recent data. Instead of extending the training data by appending new observations to history, the size of the training dataset remains fixed and only the most recent observations are held for training. Let $R \in \mathbb{N}^+$ be a hyperparameter representing the number of market-days in the rolling training window. When combined with a recalibration interval of T days, after forecasting is complete the most-recent observations from the new T-day interval replace the oldest training observations and the model is trained from scratch on the reduced history.

(3) **Rolling fine-tuning windows.** Rolling fine-tuning windows (FT) extend the idea of

Figure 4.1: Quarterly distributions of Chicago Hub DA-LMPs and natural gas spot prices over time. The left-y-axis and histograms show the distribution of Chicago Hub DA-LMPs aggregated quarterly. The right-y-axis and black dots-and-flyers show quarterly aggregate natural gas prices at TETCO-M3 where the dots represent the mean price. The upper and lower flyers represent the 75^{th} and 25^{th} percentiles respectively.

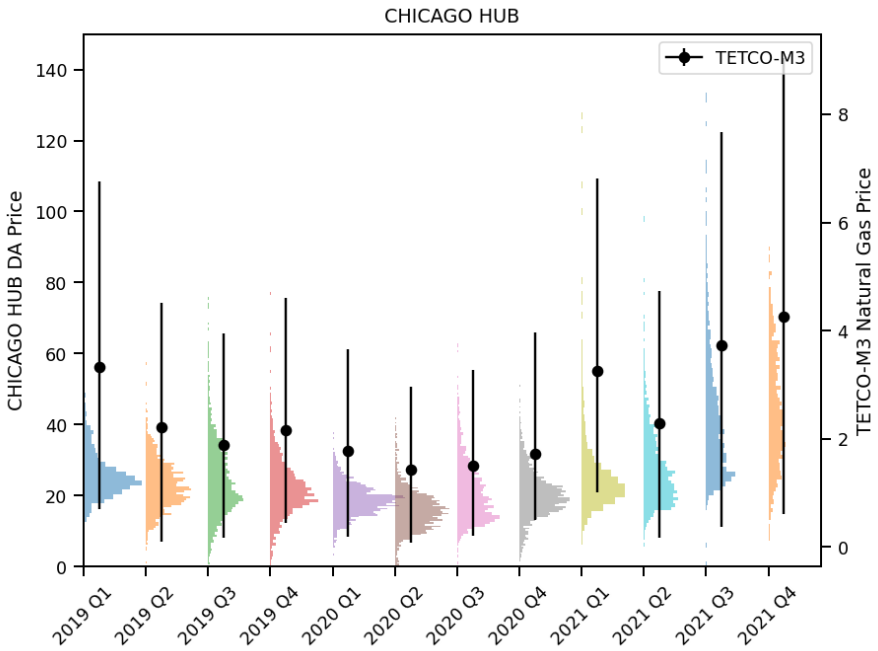

Figure 4.2: Weekly averaged Chicago Hub DA-LMPs v.s. PJM total load forecasts. The left-y-axis and blue curve show the total load forecast in PJM averaged weekly. The right-y-axis and orange curve show the Chicago Hub DA-LMP averaged weekly.

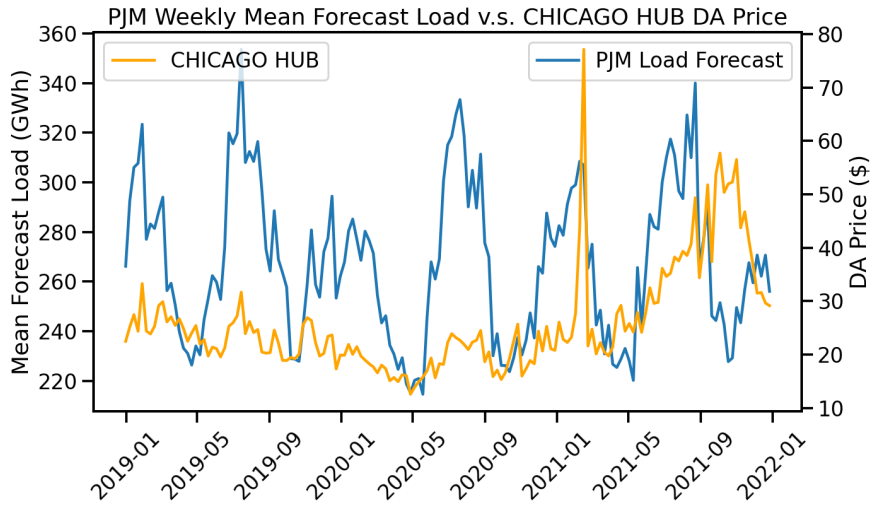

Figure 4.3: Weekly averaged Chicago Hub DA-LMPs v.s. PJM total wind generation forecasts. The left-y-axis and blue curve show the total wind generation forecast in PJM averaged weekly. The right-y-axis and orange curve show the Chicago Hub DA-LMP averaged weekly.

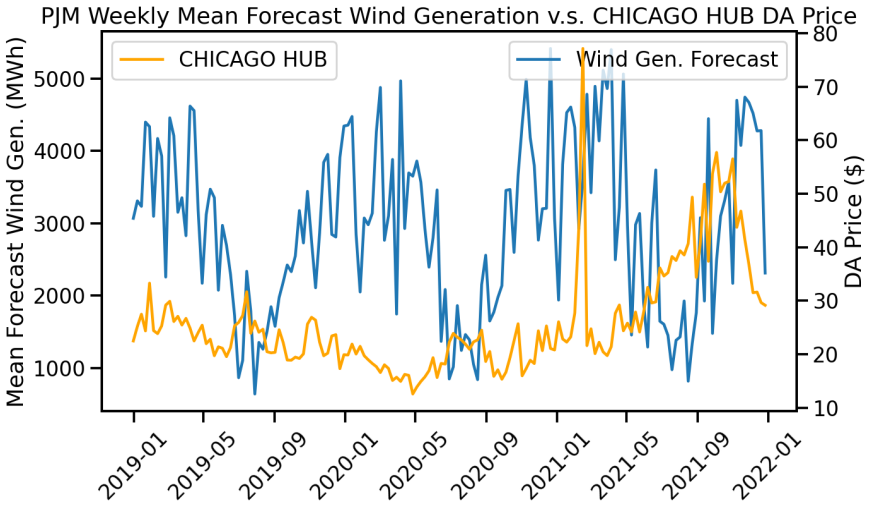

rolling training windows, however, without reducing the size of the training dataset. Let $R \in \mathbb{N}^+$ be a hyperparameter representing the number of market-days in the rolling fine-tuning window. Just like in parameter recalibration, forecasts are produced for T-day intervals whose observations are then appended to the training data before the model is re-trained from scratch. However, after the initial round of training the model is fine-tuned by reducing the learning rate and briefly continuing training on a subset of the most recent R-days in the extended history.

These updating methods are compared against a baseline with parameters that are trained once and never updated with results in Table 4.1. Parameter recalibration is shown to improve forecasting skill as the recalibration frequency increases, suggesting that the most recent market data is substantially more predictive than older observations. This observation, coupled with short training times, makes the daily recalibration of this model a practical recommendation. Inclusion of rolling training data windows with parameter recalibration is shown to negatively impact forecasting performance, with smaller training window sizes causing substantial degradations. This is likely caused by overfitting on the smaller training windows leading to reduced out-of-sample performance. Use of the fine-tuning strategy, however, greatly improves performance. Observing mCRPS metrics, reducing the fine-tuning window size yields more accurate forecasts, which is likely explained by the fine-tuning emphasizing relevant (in this case the mose recent) historical observations and further suggests that the most recent data has the most predictive power. We believe further refinement of the fine-tuning methodology, in terms of identifying and selecting the "most relevant" data points aside from those most recently observed, can likely lead to more performance gains.

4.2 Improving Sampling Tasks with Adversarial Loss

Next, the impact of including the adversarial loss term, $\mathcal{L}_{\text{ADV}}$, in the hybrid loss function and how it specifically affects the sampling performance of the model are investigated. The aforementioned 14-day recalibration and 14-day fine-tuning window methods are utilized in the following

Table 4.1: Evaluation metrics comparing methodologies to handle non-stationary data.

Update Method	Median NLL (-)	99% NLL (-)	mCRPS (-)
None	-26.337	86.574	10.392
PR ($T = 90$)	-41.724	65.773	9.413
PR ($T = 14$)	-44.127	**63.294**	7.508
PR + RT ($T = 14$, $R = 90$)	-47.907	283.582	8.327
PR + RT ($T = 14$, $R = 14$)	25.551	418573.25	15.43
PR + FT ($T = 14$, $R = 45$)	**-52.346**	66.59	6.686
PR + FT ($T = 14$, $R = 14$)	-49.839	65.27	**5.723**

experiments. A range of values for $\lambda_{\text{ADV}} > 0$ are swept over and compared against a baseline model without adversarial loss with results shown in Table 4.2.

The inclusion of adversarial loss improves the mCRPS metric. To investigate why, first recall the definition of the CRPS estimator (3.1) and note the sensitivity of the CRPS estimator to outliers samples. Consider the empirical c.d.f for an arbitrary distribution represented by a set of finite samples, if some samples are extreme outliers then they will carry a non-trivial mass under the tail of the distribution. Depending on the number and magnitude of the outliers this tail may over-estimate the tail of the true distribution resulting in a degraded CRPS estimation.

To illustrate this issue with an example, let $\mathcal{U} \sim \text{Gumbel}(\mu = 0, \beta = 1)$ with realizations u. The empirical c.d.f. $\hat{F}_{\mathcal{U}}$ is constructed by drawing 500 samples. A second c.d.f. $\hat{F}'_{\mathcal{U}}$ is constructed using the same examples, however, with a single outlier observation $u = 10,000$ added to the set of samples. For an observation at $y = 0$, the CRPS estimators are computed to be $\widehat{CRPS}_{\hat{F}_{\mathcal{U}}}(0) = 0.3331$ and $\widehat{CRPS}_{\hat{F}'_{\mathcal{U}}}(0) = 0.3748$ respectively. Clearly, extreme outliers have a detrimental effect on estimated CRPS metrics.

When observing the sample distribution drawn from a trained price density model, extreme outliers are not uncommon. Figure 4.4 shows 500 samples that estimate the joint density forecast between two price nodes marginalized out from a larger joint forecast. Most samples are indistinguishable from one another and located near the origin as expected, however, observe the small number of samples whose magnitudes are on the order of $\$10^7$. It is clear how these samples would

Table 4.2: Comparison of fine-tuning rolling window sizes

λ_{ADV}	Median NLL (-)	99% NLL (-)	mCRPS (-)
0	-49.839	65.27	5.723
0.1	-50.02	65.103	5.637
1	**-50.442**	65.176	5.569
10	-50.394	**62.854**	**5.309**

severely degrade the CRPS metrics of this forecast.

To determine if adversarial loss address this problem specifically, it is necessary to quantify the frequency of extreme outliers. Starting with the matrix $\mathbf{X}_t \in \mathbb{R}^{r \times n}$ representing r samples for a forecast at time t over n price nodes. The sample covariance matrix for $\mathbf{X_t}$ associated eigenvalues $\sigma_1 \dots \sigma_n$ are computed. Let the *total uncertainty* (TU) of our forecast be defined as

$$\text{TU}_{\mathbf{X_t}} = \sum_{i=1}^{n} \sqrt{\sigma_i},$$

which can be interpreted as the cumulative standard deviations in price along each orthogonal dimension in some rotated price space. Next, the *excess uncertainty* (EU) is defined as a binary indicator on the total uncertainty exceeding a set threshold,

$$\text{EU}_{\mathbf{X}_t} = \mathbb{1}_{\left[TU_{\mathbf{X}_t} \geq 1000\right]},$$

where 1000 is chosen as the threshold because day-ahead prices rarely exceed the low hundreds of dollars on more than a handful of nodes at any time, thus this threshold is expected to be rarely exceeded under normal market conditions. Counting the total excess uncertainty over all forecasts on the validation set then provides a metric for the frequency of outliers,

$$\text{Total Excess Uncertainty} = \sum_{t=1}^{T} EU_{\mathbf{X}_t}.$$

Comparison of the total excess uncertainty for various forecasting strategies are shown in Table 4.3. The inclusion of adversarial loss ($\lambda_{\text{ADV}} = 10$) reduces the occurrences of forecasts with excessive

Figure 4.4: Samples from a marginalized joint distribution forecast between WESTERN HUB and AEP GEN HUB price nodes. Note the outliers with values on the order of magnitude of $\$10^7$ which exceed both reasonable price expectations and hard price limits enforced by PJM.

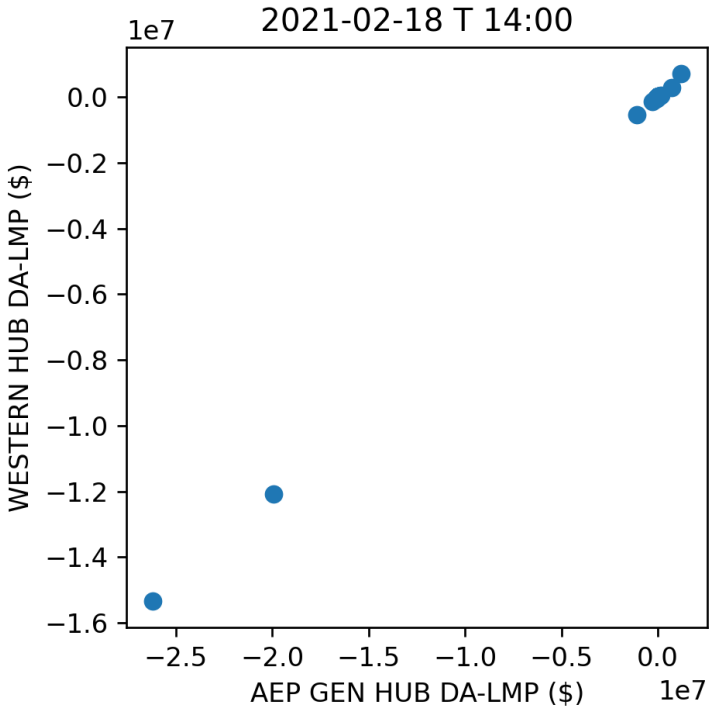

uncertainty improving the CRPS metrics forecasts.

Table 4.3: The total excessive uncertainty count is captured for four models over the evaluation dataset. Recalibration and fine-tuning sizes are both set to 14, $\lambda_{\text{ADV}} = 10$. The model denoted as *none* has no recalibration, fine-tuning, or adversarial loss. Strategies are assumed to be omitted unless specified in the model name.

Model Strategy	Total Excess Uncertainty
None	34
Recal.	180
Recal. + Fine-tune	379
Reval. + Fine-tune + Adv. Loss	72

We hypothesize this effect is due to the "contraction" of the reference density when transforming to the target density under adversarial loss due to naturally arising mode-collapse phenomena. When using a normalizing flow model as the generator of a GAN, mode-collapse can be understood as the contraction of the target density to a small neighborhood in the target-space[1] as demonstrated in Figure 4.5.

This contracting behavior is believed to regularize the mapping of the normalizing flow model in the low-density tails of the estimated target density by pulling density from the tails of the distribution in towards the modes. Figure 4.6 shows a synthetic distribution whose density transport map is learned by a normalizing flow model. The transformation of the reference domain under a push-forward mapping by a set of concentric circles drawn in the reference space and their subsequent mappings in the target space. Near the tails of the target density there is excessive warping of the reference domain as it becomes more difficult for the normalizing flow model to accurately capture low-probability tail behavior due to a lack of training observations (and also perhaps the constraints on the functional form of the affine-coupling layers). Extrapolating to higher dimensions, this warping would likely cause the occasional sample in reference space to be mapped to an outlier in the target space due to a manifestation of the curse of dimensionality.

[1] Indeed, results from the original FlowGAN work [11] show an exploding $\mathcal{L}_{\text{MLE}}$ when trained only on $\mathcal{L}_{\text{ADV}}$ despite high-quality samples still being drawn which furthers this density contraction hypothesis.

Figure 4.5: A comparison of a mode-covering and mode-collapsed density estimators. **Left:** the true multi-modal distribution. **Center:** a mode-covering Flow-GAN density estimator trained using only $\mathcal{L}_{\text{MLE}}$ loss. **Right:** a mode-collapsed Flow-GAN density estimator trained using only $\mathcal{L}_{\text{ADV}}$ loss.

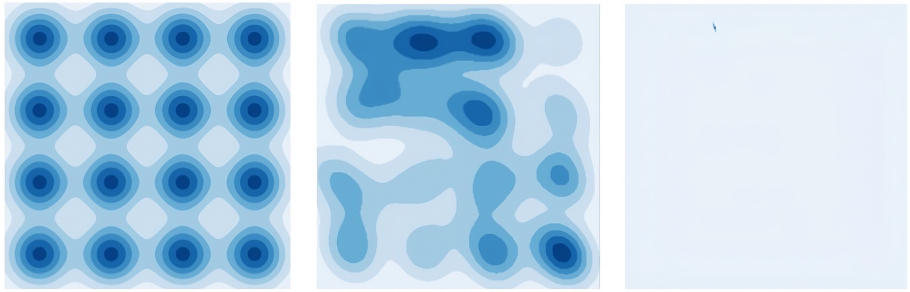

Thus, the hypothesized regularizing properties of adversarial loss would rein in excessive warping under an estimated mapping. In the context of this work it is enticing to refer to the inclusion of adversarial loss as *adversarial regularization* due to the properties observed.

4.3 Comparison Against Baselines

Finally, our proposed probabilistic forecasting methodology (cINN) — including recalibration, fine-tuning, and adversarial regularization — is compared against several baseline traditional point forecasting methods. Comparisons are first provided against two open source state-of-the-art energy price forecasting models in literature found in the `epf-toolbox` [17] python library: the modified *lasso estimated auto-regressive* (EPF-LEAR) and *deep neural network* (EPF-DNN) models as described in Section 3.4. Note, a significant downside to these models is they are only defined for single price nodes, making multi-node forecasts significantly more expensive to obtain and the resulting forecasts would likely fail sufficiently to capture the joint structure between node prices. As such, only comparisons at a select few price nodes are performed. For each price node, a single DNN model and 24 hourly LEAR models are constructed. Univariate density forecasts for each price are obtained by marginalizing out samples from the entire joint density forecast. The same training and recalibration procedures previously described are implemented for both the EPF-LEAR and EPF-DNN models, however, no rolling training or fine-tuning windows are

Figure 4.6: The mapping of the reference domain under the push-forward operation of a trained normalizing flow model with with three affine-coupling layers. **Left:** Reference samples shown in blue and concentric circles in the reference domain drawn in black. **Right:** Samples pushed-forward into the target space and the same concentric circles mapped in the target domain.

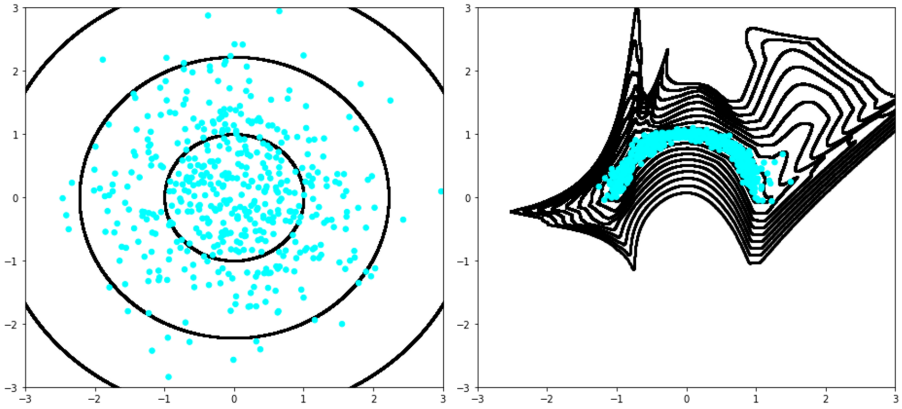

used. Comparisons between the CRPS of the probabilistic forecasts against the MAE of the EPF-DNN and EPF-LEAR forecasts are shown in Table 4.4. The proposed density forecasting method produces more accurate forecasts than state-of-the-art point forecasting methods. Note, beyond greater forecast accuracy the probabilistic forecasts also captures joint structures between price nodes and uncertainty in forecasts which non-probabilistic forecasts fail to provide.

Table 4.4: Comparison of forecast accuracy between the proposed probabilistic forecasting strategy and state-of-the-art point forecasting models from the `epf-toolbox` [17] python library over single price nodes.

Model / Price Node	EPF-LEAR (MAE)	EPF-DNN (MAE)	cINN (mCRPS)
CHICAGO HUB	6.622	6.231	**5.341**
DOMINION HUB	7.077	6.565	**6.174**
EASTERN HUB	7.095	7.526	**6.087**
NEW JERSEY HUB	4.923	5.025	**3.983**
OHIO HUB	6.444	6.119	**5.558**

Next, the proposed density forecasting methodology is compared against the commercial OPF solver. The solver only produces point forecasts on a subset of 14 of our price nodes, thus the joint density forecast on those specific nodes is marginalized out from the larger joint density. Again, the MAE of the OPF forecasts is compared against the mCRPS of the probabilistic forecasts with results shown in Table 4.5. The probabilistic forecasting strategy is more accurate than the commercial, physics-based price forecasting tool, again with the added benefit of information-rich joint probabilistic forecasts as opposed to low-information point forecasts.

Figure 4.7 illustrates forecasts from our joint density method and the three baseline methods against observed DA prices on a single node over two time intervals in 2021. Observe how the uncertainty in the probabilistic forecasts changes over time with respect to market conditions. Also note that beyond the mean forecast and 95% confidence intervals each forecast is a complex probability density function as shown in Figure 4.8.

Figure 4.7: Forecasts from the proposed probabilistic forecasting methodology, EPF-LEAR, EPF-DNN, and OPF baselines against the true NEW JERSEY HUB DA LMPs over two five-day intervals in 2021. **Left:** forecasted and observed LMPs over a five-day interval during an extreme winter weather event in Texas which caused unprecedented price action in PJM (2/12/21-2/17/21). **Right:** forecasted and observed LMPs over a five-day interval in the summer (8/13/21-8/18/21).

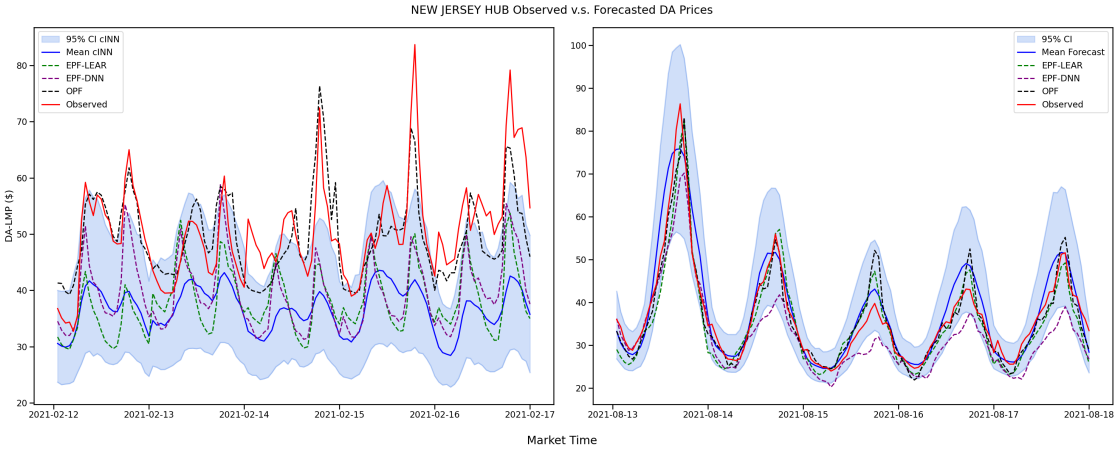

Figure 4.8: Forecasts for the proposed probabilistic forecasting methodology and EPF-LEAR, EPF-DNN, and OPF baselines against the true DA prices are shown at the NEW JERSEY HUB price node at four hours on a single market-day.

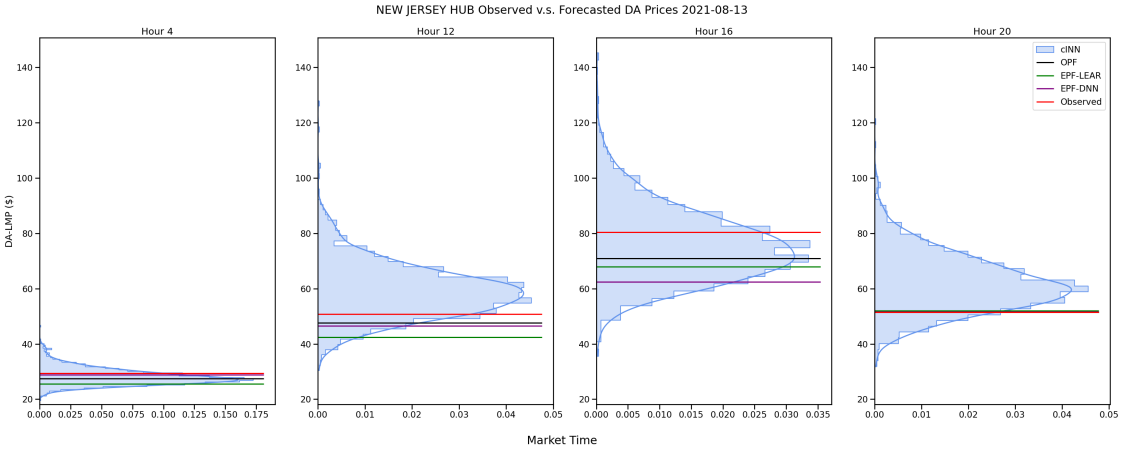

Table 4.5: Comparison of forecast accuracy between our proposed probabilistic forecasting strategy and a commercial OPF solver point forecasting product over a subset of 14 price nodes.

Model	MAE (-)	mCRPS (-)
OPF	6.666	-
cINN	-	**5.435**

Chapter 5

Conclusions

In this work we presented a novel methodology for joint probabilistic day-ahead energy price forecasts over a set of geographically distributed price nodes and several practices that can be used to improve forecasting results using recent advances in deep generative modeling. Our proposed methodology allows for both exact conditional likelihood estimation and efficient conditional sampling for forecasting tasks. Comparisons of our model to both state-of-the-art open-access benchmarks in energy price forecasting literature and commercial physics-based optimal power-flow tools provide clear evidence for the superiority of our proposed methodology both in terms of forecast accuracy and more expressive information-rich probabilistic forecasting in comparison to traditional point-forecasting methods. Despite this, we believe the methodology presented in this work can be further improved with the following lines of continued research,

(1) **Model Robustness and Interpretability**: A key issue faced during development of these methods was the use of non-standard robust metrics when tracking model fit due to the instabilities observed for mean NLL calculations caused by sporadic and extremely low log-likelihood evaluations. While workarounds were found, they do not address the root causes of these instabilities. We believe the application of modern robust deep learning methods to be a worthwhile investigation to determine if more stable results can be achieved by improving model robustness. Additionally, such techniques could be used to provide interpretability as to the quantities and market conditions to which our model is most sensitive. Such transparency is desirable for the utilization of these models when executing

positions in the markets based on information provided by these forecasts.

(2) **Hierarchical Modeling and Uncertainty Propagation**: A key assumption of our methods is that the quantities we condition our forecasts on have no uncertainty; however, load, generation, and meteorological forecasts are known to be uncertain and error-prone. While more accurate forecasts would likely improve results, no forecast is 100% correct, 100% confident, 100% of the time. Instead, capturing the uncertainty of those upstream fundamental forecasts in a separate density function $p(c_t)$ and constructing a hierarchical density estimate $p(x_t|c_t)p(c_t)$ may better capture the relationship between our fundamental forecasts and resulting price forecasts as uncertainty in fundamental forecasts can be propagated into the uncertainty of price forecasts.

(3) **Generalization to Other Markets and a Greater Number of Price Nodes**: Our experiments in this work were limited to the study of a single set of 45 price nodes in the PJM market. There are a total of 8 day-ahead energy markets in North America, with many more in Europe and the rest of the world. These markets each can have significant differences between one another in terms of regulation, available generation, load profiles, weather patterns, etc. that all have an outstanding effect on day-ahead price actions. Additionally, we only looked at a small set of 45 price nodes despite markets often being comprised of hundreds if not thousands of distinct price nodes. Further research into the generalizability of our proposed methods into other markets and the issues faced when scaling up forecasts to larger sets of price nodes are believed to be of great practical importance to the deployment and execution of this methodology.

Bibliography

[1] José Andrade, Jorge Filipe, Marisa Reis, and Ricardo Bessa. Probabilistic price forecasting for day-ahead and intraday markets: Beyond the statistical model. Sustainability, 9:1990, 10 2017.

[2] Lynton Ardizzone, Jakob Kruse, Carsten Lüth, Niels Bracher, Carsten Rother, and Ullrich Köthe. Conditional invertible neural networks for diverse image-to-image translation, 2021. arXiv:2105.02104.

[3] POWER Committee. The timeline and events of the february 2021 texas electric grid blackouts, July 2021.

[4] Eike Cramer, Dirk Witthaut, Alexander Mitsos, and Manuel Dahmen. Multivariate probabilistic forecasting of intraday electricity prices using normalizing flows, 2023. arXiv:2205.13826.

[5] Laurent Dinh, Jascha Sohl-Dickstein, and Samy Bengio. Density estimation using real nvp, 2017. arXiv:1605.08803.

[6] Jonathan Dumas, Antoine Wehenkel, Damien Lanaspeze, Bertrand Cornélusse, and Antonio Sutera. A deep generative model for probabilistic energy forecasting in power systems: normalizing flows. Applied Energy, 305:117871, 2022.

[7] Xinbo Geng and Le Xie. Learning the lmp-load coupling from data: A support vector machine based approach. IEEE Transactions on Power Systems, 32(2):1127–1138, 2017.

[8] Xavier Glorot and Y. Bengio. Understanding the difficulty of training deep feedforward neural networks. Journal of Machine Learning Research - Proceedings Track, 9:249–256, 01 2010.

[9] Tilmann Gneiting and Adrian E Raftery. Strictly proper scoring rules, prediction, and estimation. Journal of the American Statistical Association, 102(477):359–378, 2007.

[10] Ian J. Goodfellow, Jean Pouget-Abadie, Mehdi Mirza, Bing Xu, David Warde-Farley, Sherjil Ozair, Aaron Courville, and Yoshua Bengio. Generative adversarial networks, 2014. arXiv:1406.2661.

[11] Aditya Grover, Manik Dhar, and Stefano Ermon. Flow-gan: Combining maximum likelihood and adversarial learning in generative models, 2018. arXive:1705.08868.

[12] Vassilis Kekatos, Georgios B. Giannakis, and Ross Baldick. Online energy price matrix factorization for power grid topology tracking. IEEE Transactions on Smart Grid, 7(3):1239–1248, 2016.

[13] Diederik P. Kingma and Jimmy Ba. Adam: A method for stochastic optimization, 2017. arXiv:1412.6980.

[14] Ivan Kobyzev, Simon J.D. Prince, and Marcus A. Brubaker. Normalizing flows: An introduction and review of current methods. IEEE Transactions on Pattern Analysis and Machine Intelligence, 43(11):3964–3979, nov 2021.

[15] S. Kullback and R. A. Leibler. On Information and Sufficiency. The Annals of Mathematical Statistics, 22(1):79 – 86, 1951.

[16] Jesus Lago, Fjo De Ridder, and Bart De Schutter. Forecasting spot electricity prices: Deep learning approaches and empirical comparison of traditional algorithms. Applied Energy, 221:386–405, 2018.

[17] Jesus Lago, Grzegorz Marcjasz, Bart De Schutter, and Rafał Weron. Forecasting day-ahead electricity prices: A review of state-of-the-art algorithms, best practices and an open-access benchmark. Applied Energy, 293:116983, 2021.

[18] Takeru Miyato, Toshiki Kataoka, Masanori Koyama, and Yuichi Yoshida. Spectral normalization for generative adversarial networks, 2018. arXive:1802.05957.

[19] Peru Muniain and Florian Ziel. Probabilistic forecasting in day-ahead electricity markets: Simulating peak and off-peak prices. International Journal of Forecasting, 36(4):1193–1210, 2020.

[20] Ana Radovanovic, Tommaso Nesti, and Bokan Chen. A holistic approach to forecasting wholesale energy market prices. IEEE Transactions on Power Systems, 34(6):4317–4328, 2019.

[21] Kavita Surana and Sarah M. Jordaan. The climate mitigation opportunity behind global power transmission and distribution. Nature Climate Change, 9(9):660–665, Sep 2019.

[22] Bartosz Uniejewski, Jakub Nowotarski, and Rafał Weron. Automated variable selection and shrinkage for day-ahead electricity price forecasting. Energies, 9(8), 2016.

[23] Bartosz Uniejewski and Rafał Weron. Regularized quantile regression averaging for probabilistic electricity price forecasting. Energy Economics, 95:105121, 2021.

[24] Bartosz Uniejewski, Rafał Weron, and Florian Ziel. Variance stabilizing transformations for electricity spot price forecasting. IEEE Transactions on Power Systems, 33(2):2219–2229, 2018.

[25] Long Wang, Zijun Zhang, and Jieqiu Chen. Short-term electricity price forecasting with stacked denoising autoencoders. IEEE Transactions on Power Systems, 32(4):2673–2681, 2017.

[26] Yang Yang, Takashi Nishikawa, and Adilson E. Motter. Small vulnerable sets determine large network cascades in power grids. Science, 358(6365), nov 2017.

[27] Yuichi Yoshida and Takeru Miyato. Spectral norm regularization for improving the generalizability of deep learning, 2017. arXive:1705.10941.

[28] Michaël Zamo and Philippe Naveau. Estimation of the continuous ranked probability score with limited information and applications to ensemble weather forecasts. Mathematical Geosciences, 50(2):209–234, Feb 2018.

[29] Zhongxia Zhang and Meng Wu. Energy price prediction considering generation bids variation: A two-stage convolutional long short-term memory approach. In 2022 IEEE Power Energy Society General Meeting (PESGM), pages 1–5, 2022.

[30] Zhongxia Zhang and Meng Wu. Predicting real-time locational marginal prices: A gan-based approach. IEEE Transactions on Power Systems, 37(2):1286–1296, 2022.

[31] Qun Zhou, Leigh Tesfatsion, and Chen-Ching Liu. Short-term congestion forecasting in wholesale power markets. IEEE Transactions on Power Systems, 26(4):2185–2196, 2011.

[32] Jizhong Zhu. Optimization of Power System Operation. Wiley-IEEE Press.

Appendix A

List of PJM Price Nodes

Day-ahead hourly LMPs from 2019, 2020, and 2021 were collected from the following 45 PJM nodes,

(1) AECO RESID AGG
(2) AEP GEN HUB
(3) AEP-DAYTON HUB
(4) AEPAPCO RESID AGG
(5) AEPIM RESID AGG
(6) AEPKY RESID AGG
(7) AEPOHIO RESID AGG
(8) APS RESID AGG
(9) ATSI GEN HUB
(10) BGE RESID AGG
(11) CHICAGO GEN HUB
(12) CHICAGO HUB
(13) COMED RESID AGG
(14) DAY RESID AGG
(15) DEOK RESID AGG
(16) DOMINION HUB
(17) DOM RESID AGG
(18) DPLEASTON RESID AGG
(19) DPL RESID AGG
(20) DUQ RESID AGG
(21) EASTERN HUB
(22) EKPC RESID AGG
(23) FEOHIO RESID AGG
(24) HUDSONTP
(25) IMO
(26) JCPL RESID AGG
(27) LINDENVFT
(28) METED RESID AGG
(29) MISO
(30) N ILLINOIS HUB
(31) NEPTUNE
(32) NEW JERSEY HUB
(33) NYIS
(34) OHIO HUB

(35) OVEC RESID AGG

(36) PECO RESID AGG

(37) PENELEC RESID AGG

(38) PENNPOWER RESID AGG

(39) PPL RESID AGG

(40) PSEG RESID AGG

(41) RECO RESID AGG

(42) SMECO RESID AGG

(43) UGI RESID AGG

(44) VINELAND RESID AGG

(45) WESTERN HUB

Appendix B

List of PJM Load Zones

Hourly load forecasts from 2019, 2020, and 2021 were collected from the following 25 PJM zones,

(1) AECO
(2) AEP
(3) AP
(4) ATSI
(5) BGE
(6) COMED
(7) DAYTON
(8) DEOK
(9) DOMINION
(10) DPL
(11) DUQUESNE
(12) EKPC (PJMISO)
(13) JCPL
(14) METED
(15) MID-ATLANTIC REGION
(16) PECO
(17) PENELEC
(18) PEPCO
(19) PPL
(20) PSEG
(21) RECO
(22) RTO COMBINED
(23) SOUTHERN REGION
(24) UGI
(25) WESTERN REGION

Appendix C

List of NOAA Weather Stations

Hourly wind speed, temperature, and dew-point forecasts from 2019, 2020, and 2021 were collected from the following 52 NOAA weather stations,

(1) DE - Wilmington/Airport

(2) IN - Fort Wayne/Baer Field

(3) IN - Indianapolis/Intl/NWSFO

(4) IN - Lafayette/Purdue University/ASO

(5) IN - South Bend/St. Joe

(6) IN - Terre Haute/Hulman

(7) KY - Covington/Cincinnati

(8) KY - Lexington/Bluegrass

(9) KY - Louisville/Standiford

(10) MD - Annapolis

(11) MD - Baltimore (until 1979)

(12) MD - Baltimore/Science Center

(13) MI - Ann Arbor/Municipal

(14) MI - Bad Axe/Memorial

(15) MI - Detroit/City Airport

(16) MI - Detroit/Metropolitan

(17) MI - Grand Rapids/Intl/NWSFO

(18) MI - Houghton Lake/Airport

(19) MI - Kalamazoo/Intl Arpt

(20) MI - Lansing/Capital

(21) MI - Sault Ste Marie/Sanderson

(22) MI - Traverse City/Cherry

(23) NC - Charlotte/Douglas

(24) NC - Raleigh/Durham

(25) NJ - Atlantic City/Intl

(26) NJ - Newark/Intl

(27) NJ - Trenton/Mercer County

(28) OH - Akron

(29) OH - Akron-Canton/Regional

(30) OH - Cincinnati/Lunken

(31) OH - Cleveland/Hopkins/NWSFO

(32) OH - Columbus/Port Columbus Intl

(33) OH - Dayton/James M Cox Municipal

(34) OH - Dayton/Wright-Patterson AFB

(35) OH - Toledo Express

(36) OH - Toledo/Metcalf Field

(37) PA - Allentown-Bethlehem

(38) PA - Erie/Intl

(39) PA - Harrisburg Intl

(40) PA - Philadelphia/Intl

(41) PA - Pittsburgh/Intl

(42) PA - Wilkes-Barre/Scranton

(43) PA - Williamsport

(44) VA - Norfolk/Intl Arpt

(45) VA - Richmond/Byrd Field

(46) VA - Richmond/Hanover

(47) VA - Roanoke/Municipal

(48) VA - Wallops Island/Station

(49) VA - Washington/Dulles Intl Arpt

(50) WV - Charleston/Kanawha

(51) WV - Elkins/Randolph Field

(52) WV - Huntington/Tri State

Appendix D

Model and Optimizer Hyperparameters

D.1 cINN

For all experiments we construct our cINN normalizing flow generator as follows,

Table D.1: Fixed hyperparameters of the cINN generator model.

Parameter Name	Value
Reference Distribution	Standard Multivariate Gaussian
# Flow Layers	12
Flow NN Hidden Layers	1
Flow NN Hidden Units	128
Flow NN Activation	ReLU
Feature Extraction Network	Omitted[1]
p-Dropout	0.8
Spectral Norm Regularization [27]	0.1
Weight Initialization	Uniform Xavier [8]

Additionally, we used a soft-clamping on the outputs of the s_1 and s_2 neural networks in each flow layer $\tilde{s} = \frac{2\alpha}{\pi} \arctan\left(\frac{s}{\alpha}\right)$ to prevent exploding values from exponentiation. We take $\alpha = 1.9$ as recommended [2].

[1] We experimented with many settings for a deep feed-forward neural network projecting into both higher and lower dimensional latent feature spaces, however, we found that inclusion of the feature extraction neural network tended to significantly increase NLL metrics while degrading mCRPS metrics. We believe a valuable line of future work to be further investigation of the root cause of the divergence between these metrics and methods for reducing the gap.

D.2 GAN Discriminator

For all experiments we construct a feed-forward spectral-normalized [18] GAN discriminator as follows,

Table D.2: Fixed hyperparameters of the SN-GAN discriminator model.

Parameter Name	Value
Activation	LeakyReLU($\alpha = 0.2$)
Hidden Layer %[2]	[0.8, 0.4, 0.2, 0.1]

D.3 EPF-DNN

We construct a modified version deep neural network presented in the open-access `epf-toolbox` used in the experiments of section 4.3 as follows,

Table D.3: Fixed hyperparameters of the EPF-DNN model.

Parameter Name	Value
# Hidden Layers	1
# Hidden Units / Layer	512
Activation	LeakyReLU
p-Dropout	0.4
Spectral Norm Regularization	0.01

D.4 Adam Optimizer

All deep-learning models are trained using the Adam optimizer with parameters as follows,

[2] The number of hidden units per layer is calculated as a percentage of the number of input (# of price nodes + # conditional quantities), i.e. $\texttt{hidden size}_i = \texttt{input size} \times \texttt{hidden pct}_i$.

Table D.4: Fixed hyperparameters of Adam optimizers.

Parameter Name	Value
β_1	0.9
β_2	0.98
Learning Rate	10^{-3}
Fine-tune Learning Rate	10^{-4}
Batch Size	128